Optimized Planar Transformer for a Multi-Output LLC Converter

Cédric Colonna
POWCOMA
Marseille, France
cedric.colonna@powcoma.com

Lucien Lecocq
Airbus Defence and Space
Élancourt, France

Patrick Dubus
POWERLOGY
Saint-Forget, France
patrick.dubus@powerlogy.fr

***Abstract*—This paper presents the design, optimization and validation of a planar transformer for a $203\,\mathrm{W}$ multi-output LLC resonant converter operating from a $36\,\mathrm{V}$ input with two secondary outputs at $12\,\mathrm{V}$ and $30\,\mathrm{V}$. The proposed approach is a systematic optimization of the winding arrangement based on the spatial control of the magnetomotive force (MMF) distribution inside the winding window: windings are assigned to printed-circuit-board layers so as to minimize the stored leakage energy, that is, the integral of the squared field intensity along the stack-up. In a multi-output structure this objective cannot be a single scalar, since each secondary imposes its own leakage constraint; it is therefore posed on the full leakage matrix of the four-winding structure under manufacturing and creepage constraints. The method combines MMF shaping, multilayer interleaving optimization, two-dimensional extraction of the winding resistances and of the inter-winding capacitance, and three-dimensional finite-element validation on an ER32 ferrite core. Core losses are evaluated by finite-element integration with a data-driven material model applied element by element to the flux-density map; separating the effects at play shows that the waveform assumption of the manufacturer's curves and the choice of volume basis each weigh about $20\,\%$, whereas resolving the flux distribution spatially changes the result by only $2\,\%$. A comparative loss analysis against the measured impedances of the previous litz-wire transformer gives a predicted loss reduction of $50\,\%$ at constant architecture and $52\,\%$ including the removal of one output rail. The results confirm that direct optimization of the magnetic field distribution is an effective strategy for high power density planar LLC transformers, in particular under asymmetrical multi-output loading. The one-month interval allowed for the manuscript did not permit the experimental campaign to be completed; it is under way and its results will be presented at the conference. This study is part of the ADHA (Advanced Data Handling Architecture) project.**

***Index Terms*—planar transformer, LLC converter, magnetomotive force optimization, multi-output converter, finite element modeling, leakage matrix, data-driven core loss.**

I. Introduction

Planar magnetic components are widely used in high power density LLC resonant converters because of their low profile, their geometric reproducibility and their compatibility with automated manufacturing. Their performance is however governed by the distribution of the leakage flux in the winding window, by proximity losses and by inter-layer coupling [1]–[3]. The dependence of leakage inductance on the winding arrangement has been analysed extensively for two-winding planar structures [4]–[6], and automated layer-assignment tools based on one-dimensional MMF models have recently been proposed [7].

Multi-output resonant converters raise a different problem. The output powers are strongly asymmetric, so the ampere-turn contribution of each secondary to the MMF profile differs by an order of magnitude; and the design is no longer constrained by a single leakage value but by a set of leakage inductances, one per secondary, each of which affects a different system-level requirement. Planar multi-output resonant transformers have been demonstrated before [8]–[13], but the interaction between the layer assignment and the full leakage matrix has received little attention.

This paper reports the replacement of a qualified litz-wire transformer by a planar structure in the LLC stage of the ADHA power module. The contribution is threefold:

- the layer-assignment problem is formulated on the *leakage matrix* of a four-winding structure, under printed-circuit-board (PCB) manufacturing, via-current and creepage constraints, rather than on a single scalar objective;
- core losses are evaluated by applying a neural-network material model from the MagNet Challenge [14], [15] *element by element* on the three-dimensional flux-density map; the error of the classical approach is decomposed into a waveform term, a volume-basis term and a spatial-averaging term, and the last one—the one the method was built to capture—turns out to be the smallest;
- the loss reduction relative to the litz baseline is decomposed into its physical contributors instead of being reported as a single figure, and the increase of the inter-winding capacitance and its effect on the conducted common-mode (CM) budget are assessed against the existing, already-qualified CM filter.

The transformer is designed for a $203\,\mathrm{W}$ LLC converter operating at its series resonant frequency, with fixed input and output voltages. The requirements are summarized in Table I.

II. Reference Design and Measured Baseline

The existing engineering model (EM) uses a litz-wire transformer with three secondary rails ($5\,\mathrm{V}$, $12\,\mathrm{V}$, $28\,\mathrm{V}$) operated at $200\,\mathrm{kHz}$, the $28\,\mathrm{V}$ rail being obtained from a linear regulator fed by a rectified $30\,\mathrm{V}$ winding. Cross-regulation between the $5\,\mathrm{V}$ and $12\,\mathrm{V}$ outputs constrains the turns ratios. In the

TABLE I: LLC Transformer Specification

Parameter	Symbol	Value
Input voltage	V_{in}	36 V
Total output power	P_{out}	203 W
Output 1 (center-tapped)	–	12 V / 173 W
Output 2 (bridge rect.)	–	30 V / 30 W
Turns ratio	–	3 : 2×2 : 5
Switching frequency	F_s	400 kHz
Magnetizing inductance	L_m	20 μH
Core	–	ER32/6/25, 3C95
Core effective area	A_e	141 mm^2
Core effective volume	V_e	5386 mm^3
PCB	–	12 layers, 70 μm Cu

TABLE II: Measured Characteristics of the Litz-Wire Baseline

Quantity	Pri	12P	12M	5P	5M	28P	28M
R_{DC} (mΩ)	9.2	12	13	8	7.75	285	242
R_{AC} (mΩ)†	22	16	16.5	9	10	405	425
$R_{\mathrm{AC}}/R_{\mathrm{DC}}$	2.4	1.33	1.27	1.13	1.29	1.41	1.76
L_f (nH)	540	210	205	110	102	660	720

†measured at 200 kHz.

proposed architecture the 5 V rail is generated by a qualified point-of-load converter, which removes two windings and relaxes the turns-ratio constraint.

The litz transformer was characterized on an impedance analyser; Table II gives the results, which set the reference against which the planar design is assessed. Two observations drive the redesign. The winding resistances are high with respect to the target efficiency: litz wire gives a favourable $R_{\mathrm{AC}}/R_{\mathrm{DC}}$ ratio at the cost of the copper fill factor in the winding window [16]. And the secondary leakage inductances, in the 100–700 nH range, cause overvoltages on the synchronous rectifiers and require snubbers.

The measurements confirm that the coupling inside the litz structure is poor. The primary $R_{\mathrm{AC}}/R_{\mathrm{DC}}$ of 2.4 at 200 kHz is far above what a litz bundle alone would give, and the leakage inductances of every winding are in the hundreds of nanohenries. Both observations point to the same cause: the windings are wound in successive layers with little interleaving, so the magnetomotive force builds up across the window instead of being cancelled.

Combining these measured impedances with the RMS currents of the nominal operating point gives the loss breakdown of Table III, which is the experimental reference used throughout this paper. Each winding loss is computed as $R_{\mathrm{DC}}I_{DC}^2 + R_{\mathrm{AC}}I_{AC}^2$ from the measured values of Table II, the 200 kHz resistance being applied to the fundamental of the rectified current. Core losses of 200 mW are obtained from the turns count and the core cross-section. The resulting total is 8.71 W, of which more than half is dissipated in the primary alone.

TABLE III: Operating Currents and Losses of the Litz-Wire Baseline, Derived from the Measured Impedances of Table II

Quantity	Pri	12P	12M	5P	5M	28P	28M
I_{DC} (A)	0	8.96	–	3.58	–	0.72	–
I_{AC} (A)†	14.4	5.98	–	2.39	–	0.48	–
Loss (W)	4.560	1.540	1.633	0.153	0.156	0.241	0.223

†fundamental, 200 kHz. Core loss 0.200 W; total 8.706 W.

III. MMF-Based Layer Assignment

A. Leakage Energy and Leakage Matrix

The winding window is described by the coordinate x normal to the layers. For a stack of conductive layers of thickness e_{cu} separated by dielectric of thickness e_{iso}, the tangential field is piecewise constant and given by the cumulated ampere-turns,

$$H(x) = \frac{1}{b_w} \sum_{k\,:\,x_k \le x} n_k\, i_k, \tag{1}$$

where b_w is the breadth of the window, n_k the number of turns carried by layer k and i_k its current. The magnetostatic energy stored in the leakage field follows as

$$W_{\mathrm{lk}} = \frac{\mu_0}{2}\, S_w \int_0^{h_w} H^2(x)\,\mathrm{d}x \simeq \frac{\mu_0}{2}\, S_w \sum_j H_j^2\, \Delta x_j, \tag{2}$$

where h_w is the total stack height and $S_w = b_w\, l_w$ the cross-section of the winding window normal to x, l_w being the mean turn length. Equation (2) is the classical one-dimensional result [1], [17]; the discrete form weights each interval by its *thickness* Δx_j, not by its position.

For a two-winding transformer, minimizing W_{lk} is equivalent to minimizing the leakage inductance and a single scalar objective is sufficient. This is not the case here. The structure has four electrically distinct windings (primary, 12V1, 12V2, 30V) and the relevant quantity is the leakage matrix obtained from the pairwise short-circuit energies,

$$L_{\mathrm{lk}}^{(i,j)} = \frac{2\, W_{\mathrm{lk}}^{(i,j)}}{I_i^2}, \tag{3}$$

where $W_{\mathrm{lk}}^{(i,j)}$ is the energy stored when winding i is excited and winding j is short-circuited. Each coefficient maps onto a different system-level requirement:

- $L_{\mathrm{lk}}^{(p,12)}$ enters the resonant tank and therefore sets the resonant capacitor and the gain characteristic;
- $L_{\mathrm{lk}}^{(12P,12M)}$ governs the overvoltage on the synchronous rectifiers and determines whether the secondary snubbers can be removed;
- $L_{\mathrm{lk}}^{(p,30)}$ contributes to the cross-regulation of the rectified 30 V rail.

The design problem is therefore a constrained one—each coefficient must lie inside its own interval—and not the minimization of a single figure of merit. This is the point where a multi-output structure departs from the two-winding formulations of [4], [7].

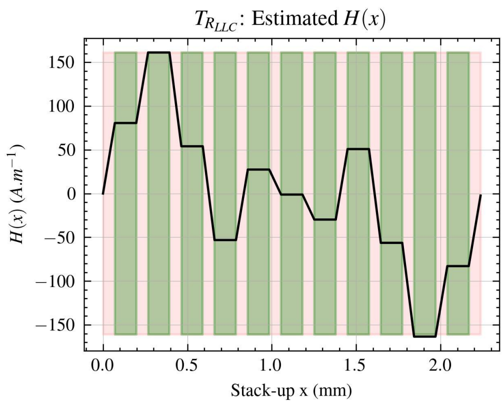

Fig. 1: Magnetic field intensity along the stack-up coordinate for the selected arrangement. Green bands mark the PCB dielectric, the narrow pink intervals between them the copper layers, across which H ramps. $H(x)$ returns to zero at both window boundaries, which verifies the ampere-turn balance.

TABLE IV: Leakage Inductances and Coupling Factors, 1-D Model

Quantity	**Primary**	**12 V**	**30 V**
L_f (nH)	20.4	5.45	77
Coupling factor k	0.990	0.990	0.986

B. Constrained Combinatorial Assignment

The turns allocation follows from the RMS currents: six layers for the primary, arranged as three turns in series duplicated in parallel; four layers for the two 12 V windings; two layers for the 30 V winding. Assigning these windings to the twelve layers is a permutation problem over a multiset. The search space is small enough for exhaustive enumeration, which removes the need for the metaheuristics used in [7], provided the following constraints are enforced:

- the two 12 V layers of a same rail are kept adjacent, so that $L_{\text{lk}}^{(12P,12M)}$ is minimized and the secondary snubbers can be removed;
- the 30 V winding, which contributes little to the ampere-turn balance, is placed at the centre of the stack;
- high-current interconnections are routed outside the winding area to avoid current crowding close to the core limb;
- layer separation and creepage follow the PCB stack-up qualified for the platform (130 μm between layers, 70 μm copper); via count and per-via current are constrained so that the temperature rise in any via stays below 10 K.

The MMF profile of the selected arrangement is shown in Fig. 1 and the arrangement itself in Fig. 2. The field returns to zero at both ends of the window, which verifies the ampere-turn balance, and the residual excursion is confined to the outer primary layers. The leakage inductances and coupling factors predicted by (2)–(3) are given in Table IV.

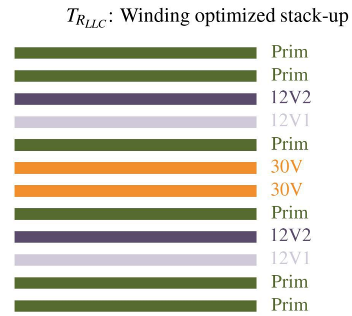

Fig. 2: Resulting winding-to-layer assignment on the twelve-layer board. The two 12 V rails are adjacent and the 30 V winding occupies the two central layers.

C. Turn Geometry Inside a Layer

Within a layer, the radii of the concentric turns are chosen in geometric progression so as to equalize the DC resistance of each turn, following the classical result of Huang and Ngo [18]:

$$r_i = \left(r_1^{k-i}\, r_{\max}^{i}\right)^{1/k}, \qquad i = 1 \dots k. \tag{4}$$

At 400 kHz the copper skin depth is 104 μm, i.e. larger than the 70 μm layer thickness. Skin effect inside a layer is therefore weak and the loss amplification is dominated by proximity effects, which justifies acting on the MMF profile rather than on the conductor thickness. Consequently (4), which is a DC-optimal result, is not exactly optimal at the operating frequency; the resulting R_{AC} is evaluated by finite elements in Section IV-B.

The transformer resulting from Sections III-B and III-C is shown in Fig. 3. The primary consists of separate turns, the third turn being obtained by rotating the first about the y axis. Each 12 V secondary is a single turn looping back on the outside of the transformer, duplicated and reversed to form the two turns, the two mid-points being electrically isolated from each other. The 30 V winding occupies the two central layers with 2.5 turns each. All vias have a diameter of 0.4 mm and are sized for 2 A.

IV. Three-Dimensional Finite-Element Validation

A. Simulation Plan

Four simulation sets were run, the AC ones at 400 kHz:

1) each winding excited alone at low frequency, giving the DC resistance including vias and the self-inductance; the primary is additionally excited with the nominal magnetizing current to obtain the flux density in the core;
2) each winding excited with one other winding short-circuited, giving the leakage matrix (3) and the associated AC resistance;
3) the nominal operating configuration, in which the 30 V winding and one of the two 12 V windings conduct

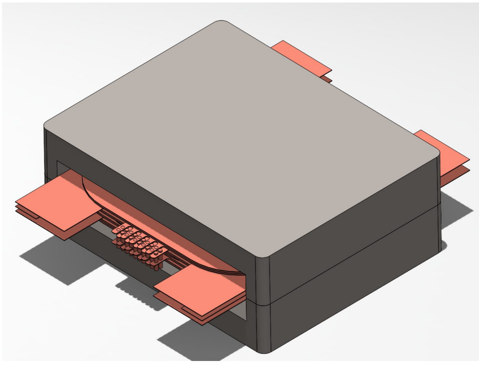

Fig. 3: Three-dimensional model of the proposed planar transformer, top view, upper core half removed. High-current interconnections and via fields are placed outside the winding area.

simultaneously with the primary, giving the loss distribution;

4) an electrostatic model without the core, giving the primary-to-secondary capacitance.

Representative results of sets 1 and 3 are shown in Fig. 4.

B. Winding Resistances

Table V compares the analytical estimate, the two-dimensional extraction and the three-dimensional result. The analytical estimate assumed $R_{\mathrm{AC}}/R_{\mathrm{DC}} = 2$ for the primary and 1.5 for the secondaries. The three-dimensional simulation gives a higher ratio on the primary, a direct consequence of the large number of layers and of the very good inter-winding coupling: the arrangement reduces the stored leakage energy, not the proximity field seen by the primary layers themselves. This is the practical limit of using (2) alone as a design criterion, and it is consistent with the longitudinal/transversal flux decomposition of [6].

Vias were modelled as solid conductors. A plated barrel of $70\,\mu\mathrm{m}$ on a $0.4\,\mathrm{mm}$ hole through a $2.2\,\mathrm{mm}$ board gives $1\,\mathrm{m}\Omega$ per via, hence $171\,\mu\Omega$ per winding once paralleled: about $5\,\%$ of the winding DC resistance, included below.

C. Leakage Matrix

Table VI reports the short-circuit results, the rows corresponding to the excited winding and the columns to the short-circuited one. The primary leakage is essentially independent of which secondary is shorted, at 20.9–21.8 nH,

TABLE V: Winding Resistances: Analytical, 2-D FE and 3-D FE

Quantity ($\mathrm{m}\Omega$)	**Pri**	**12P**	**12M**	**30P**
R_{DC} analytical	3.5	3.0	3.0	21
R_{DC} 2-D FE	3.5	4.2	4.2	26
R_{DC} 3-D FE	3.29	4.16	4.17	24.9
R_{AC} analytical	7.0	4.5	4.5	35
R_{AC} 3-D FE	8.02	4.71	4.70	29.6

TABLE VI: Leakage Matrix from 3-D FE Short-Circuit Simulations

Excited	**Quantity**	**Pri s.c.**	**12P s.c.**	**12M s.c.**	**30P s.c.**
Primary	R_{AC} ($\mathrm{m}\Omega$)	–	8.5	8.5	8.6
	L_f (nH)	–	21.8	21.7	20.9
12V P	R_{AC} ($\mathrm{m}\Omega$)	4.67	–	4.80	5.04
	L_f (nH)	9.3	–	7.48	15.0
12V M	R_{AC} ($\mathrm{m}\Omega$)	4.65	4.78	–	5.10
	L_f (nH)	9.3	7.42	–	15.8
30V	R_{AC} ($\mathrm{m}\Omega$)	29.6	31.0	30.0	–
	L_f (nH)	59.2	93.0	91.0	–

which confirms that the primary is symmetrically distributed with respect to all secondaries. The $12\mathrm{P}/12\mathrm{M}$ coefficient, at $7.5\,\mathrm{nH}$, is the lowest of the matrix and is a direct consequence of the adjacency constraint imposed in Section III-B. The $30\,\mathrm{V}$ winding shows the largest leakage, which is acceptable because it feeds a linear post-regulator and not a synchronous rectifier.

Compared with the litz baseline of Table II, the secondary leakage inductances are reduced by more than one order of magnitude ($205\,\mathrm{nH}$ to $9.3\,\mathrm{nH}$ on the $12\,\mathrm{V}$ rail). This is what allows the secondary snubbers to be removed, a system-level benefit in mass, part count and derating that the transformer loss figure alone does not capture.

D. Element-Wise Evaluation of Core Losses

The flux density in the core is markedly non-uniform (Fig. 4a), because the cross-section of the ER32 varies along the flux path and because the air gap spreads the field in its vicinity. Core-loss models—whether Steinmetz-based [19] or data-driven [20]—are formulated for a homogeneous excitation of a toroidal sample. Applying them to a shaped core therefore requires a choice of the representative flux density.

Three approaches were compared. The first uses the analytical peak flux density,

$$B_p = \frac{V_{\mathrm{in}}}{4\,N_p\,A_e\,F_s}, \tag{5}$$

which gives $53\,\mathrm{mT}$ here, together with the manufacturer's loss curves, which assume a sinusoidal excitation. The second applies a data-driven model to the volume-averaged flux density obtained from the three-dimensional simulation. The third, proposed here, treats the model as a *local constitutive loss law*: the flux-density magnitude B_e and the element volume ΔV_e are exported for every element of the core mesh, a triangular waveform $B_e(t)$ consistent with the square voltage applied by the LLC half-bridge is reconstructed on each element, and the total loss is obtained as

$$P_{\mathrm{Fe}} = \sum_e p_v(B_e(t),\, F_s,\, T)\;\Delta V_e, \tag{6}$$

where p_v is evaluated by the HARDCORE network of the MagNet Challenge [14], [15], which returns the loss density from an arbitrary $B(t)$ waveform for the material considered.

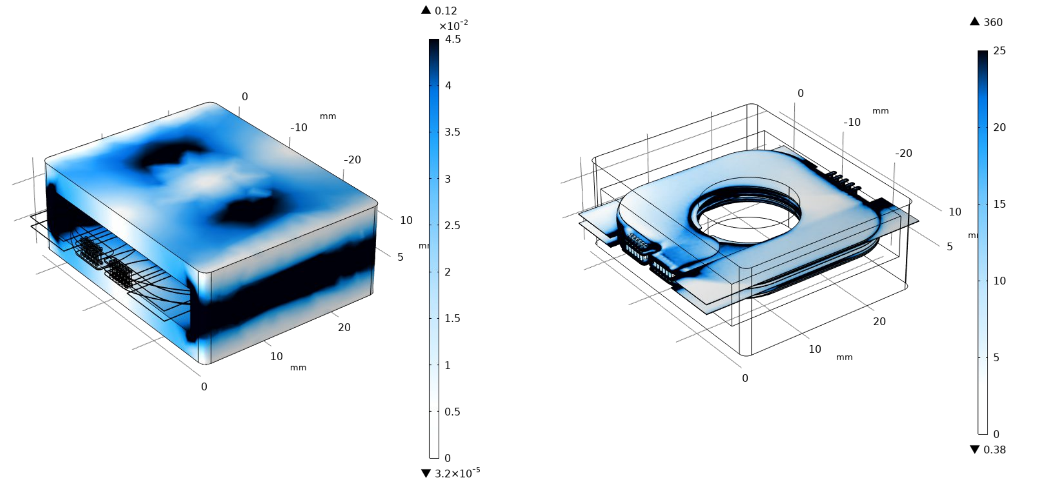

(a) Flux density magnitude in the ER32 core (T), nominal magnetizing current. The colour scale is saturated at $45\,\mathrm{mT}$; the local maximum reaches $0.12\,\mathrm{T}$.

(b) Current density magnitude in the planar windings ($\mathrm{A/mm^2}$), nominal operating point. The colour scale is saturated at $25\,\mathrm{A/mm^2}$; the local maximum, $360\,\mathrm{A/mm^2}$, occurs in the via fields and terminal transitions.

Fig. 4: Three-dimensional finite-element results. Most of the core volume operates below $45\,\mathrm{mT}$ while the local peak reaches $0.12\,\mathrm{T}$, i.e. a spread of nearly a factor of three over the core; this non-uniformity is what motivates the element-wise loss evaluation of Section IV-D. In the windings, the current density stays below $25\,\mathrm{A/mm^2}$ over the turns themselves, the peaks being confined to the interconnections placed outside the winding area.

TABLE VII: Core Loss: Separating the Three Effects

Representative B	**Loss model**	**Volume**	**P_{Fe} (mW)**
B_p from (5)	datasheet, sine	V_e	700
volume average	HARDCORE, triang.	V_e	850
volume average	HARDCORE, triang.	V_{geom}	1020
element-wise	HARDCORE, triang.	V_{geom}	1040

$V_e = 5386\,\mathrm{mm}^3$ (effective), $V_{geom} = 6461\,\mathrm{mm}^3$ (meshed geometry).

A point of definition has to be settled before these approaches can be compared, and it turns out to matter as much as the modelling itself. The datasheet and volume-averaged evaluations are carried out on the *effective* magnetic volume $V_e = A_e\, l_e = 5386\,\mathrm{mm}^3$, the lumped equivalent quoted by the manufacturer, which assumes a homogeneous field. The element-wise sum (6) runs instead over the meshed ferrite geometry, whose volume is $6461\,\mathrm{mm}^3$ for the ER32/6/25 core set, i.e. $20\,\%$ more material. Table VII therefore reports the volume basis of each evaluation explicitly, the volume-averaged case appearing twice—once on each basis—so that the three effects at play, namely waveform and material model, volume basis and flux non-uniformity, can be separated.

The result is not the one that was expected. Going from the manufacturer's sinusoidal curves to the neural-network model evaluated on a triangular waveform raises the loss by $21\,\%$; correcting the volume basis adds a further $20\,\%$; but resolving the flux distribution element by element, instead of using its volume average, adds only $2\,\%$. In other words, for this core and this operating point the non-uniformity of B is *not* what drives the discrepancy between methods, even though the flux density varies by nearly a factor of three across the core (Fig. 4a). This is consistent with Jensen's inequality, which for a convex $p_v(B)$ guarantees that the element-wise sum cannot fall below the volume-averaged evaluation on the same volume, but says nothing about the size of the gap; the $2\,\%$ obtained here indicates that the volume fraction operating far from $\langle B \rangle$ is limited. The dominant error in the classical approach is the waveform assumption, not the spatial averaging.

This conclusion is only reachable if the element volumes are handled correctly, and there is a trap worth reporting. In the finite-element package used here, the element volume is available as a field variable, but a data export on a solution dataset evaluates expressions at the mesh *nodes* while the element volume is an *element* quantity. Several nodes share the same element, so the naive sum of the exported volumes falls short of the true volume by roughly the number of tetrahedra per node—a factor of 3.3 on the mesh used here—and the computed loss is short by the same factor. Summing the exported volumes and checking the total against the geometric volume of the core, before any loss is computed, is a two-line test that should be systematic.

The network was trained on toroidal samples of fixed dimensions, under steady-state excitation and without DC bias, so its element-wise use is an extrapolation outside the training distribution and the last row of Table VII is an estimate rather than an absolute prediction.

E. Inter-Winding Capacitance and Common-Mode Budget

Planar construction improves coupling at the cost of a much larger primary-to-secondary capacitance. An electro-

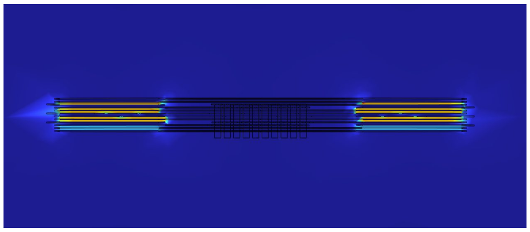

Fig. 5: Electrostatic finite-element model used to extract the primary-to-secondary capacitance (cross-section, core removed).

static finite-element model of the windings alone (Fig. 5), with $\varepsilon_r = 5$ for the dielectric, gives $C_{\mathrm{ps}} = 1.54\,\mathrm{nF}$ in two dimensions and $C_{\mathrm{ps}} = 1.05\,\mathrm{nF}$ in three dimensions, the two-dimensional value being overestimated because it ignores the actual overlap area. The three-dimensional value is retained. It compares with the $25\,\mathrm{pF}$ measured on the litz transformer, i.e. a factor of about forty.

Keeping the existing CM filter, the applicable conducted emission limit [21] at $400\,\mathrm{kHz}$ and the filter attenuation give

$$A_{CM} = 70 - 20\log_{10}\left(\frac{F_s}{300\,\mathrm{kHz}}\right) = 67.5\,\mathrm{dB}\mu\mathrm{A}, \qquad (7)$$

$$A_{F,CM} = 40\log_{10}\left(\frac{f_{c,CM}}{F_s}\right) = -44\,\mathrm{dB}. \qquad (8)$$

Circuit simulation with the extracted C_{ps} gives a common-mode current of $56\,\mathrm{mA}$ peak at the transformer, i.e. $95\,\mathrm{dB}\mu\mathrm{A}$, hence $51\,\mathrm{dB}\mu\mathrm{A}$ at the module input after filtering. The margin against (7) is therefore $16.5\,\mathrm{dB}$ and the CM filter needs no modification.

This result deserves a comment, because the raw capacitance is a poor predictor of common-mode noise. Saket *et al.* showed that a planar transformer with a capacitance sixty times larger than a wire-wound reference can nevertheless produce 15–$25\,\mathrm{dB}$ *less* common-mode noise, provided the layers are interleaved by pairs of identical $\mathrm{d}v/\mathrm{d}t$ [22]–[24]. That technique is directly applicable to a single-secondary converter. In the present case there are three distinct secondary potentials and the number of layers that can be paired collapses: enforcing the $\mathrm{d}v/\mathrm{d}t$ pairing conflicts with the adjacency and centring constraints of Section III-B. The design reported here resolves the conflict in favour of the leakage constraints, which is acceptable only because the CM filter retains $16.5\,\mathrm{dB}$ of margin.

F. Thermal Behaviour

The loss densities of the analytical breakdown were applied to a three-dimensional thermal model with the interfaces held at $20\,^\circ\mathrm{C}$ (Fig. 6). The conservative assumption was made that the thermal conductivity of the board is that of air and that the core losses are entirely injected into the windings. Even under these conditions the maximum temperature rise inside the windings is $28\,\mathrm{K}$. The model was run with the $3.4\,\mathrm{W}$ of the analytical prediction; since the problem is conduction dominated and the boundary conditions are fixed, the rise scales linearly with the dissipated power, so the $4.2\,\mathrm{W}$ of Table VIII corresponds to about $35\,\mathrm{K}$. Both values remain compatible with the derating rules applicable to the module [25], [26].

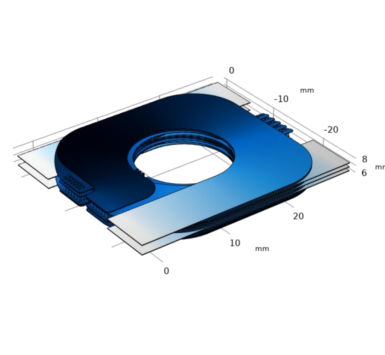

Fig. 6: Steady-state temperature (K) in the windings, interfaces held at $293\,\mathrm{K}$, board conductivity taken equal to that of air. Maximum rise $28\,\mathrm{K}$.

TABLE VIII: Loss Comparison: Measured Litz Baseline versus Predicted Planar Design

	Litz (measured Z)		**Planar (predicted)**	
Losses (W)	**as built**	**iso-arch.**	**analytical**	**3-D FE**
Primary	4.560	4.560	1.450	1.663
12V P	1.540	1.540	0.560	0.708
12V M	1.633	1.633	0.560	0.708
5V (P+M)	0.309	–	–	–
30V (P+M)	0.464	0.464	0.100	0.100
Core	0.200	0.200	0.700	1.040
Total	**8.706**	**8.397**	**3.370**	**4.219**
Gain vs. iso-arch. (%)	–	–	59.9	49.8
Gain vs. as built (%)	–	–	61.3	51.5

Litz losses are computed from the measured impedances of Table II and the operating currents of Table III. Architecture simplification (5 V removal) alone accounts for $0.309\,\mathrm{W}$, i.e. $3.5\,\%$; the remaining $4.18\,\mathrm{W}$ is attributable to the change of winding technology and operating frequency.

V. Comparative Loss Analysis

The comparison is between a litz-wire transformer whose impedances were *measured* on the engineering model (Tables II and III) and a planar transformer whose losses are *predicted*, analytically and then by three-dimensional finite elements, both levels being reported so that the spread between them can be judged.

The new design also differs from the EM in two respects at once: the $5\,\mathrm{V}$ rail is no longer produced by the transformer, and the winding technology changes from litz wire to planar with a switching frequency raised from $200\,\mathrm{kHz}$ to $400\,\mathrm{kHz}$. Reporting a single overall figure would attribute to the technology a gain that is partly due to the architecture. Table VIII therefore gives an *iso-architecture* column, in which the two $5\,\mathrm{V}$ windings are removed from the litz baseline, alongside the design as actually built.

Three observations follow. First, the analytical model underestimates the three-dimensional result by $20\,\%$ on the total, and in the same direction on both mechanisms: by $16\,\%$ on the copper, because the assumed $R_{\mathrm{AC}}/R_{\mathrm{DC}}$ ratio of 2 on the primary is optimistic for a twelve-layer stack, and by $33\,\%$ on the core, because it uses the datasheet curves under a sinusoidal assumption and on the effective rather than the geometric volume (Section IV-D). An analytical pre-design of this kind should therefore be read as a lower bound, not as a centred estimate.

Second, the dominant contribution is the primary winding, whose loss falls from $4.56\,\mathrm{W}$ to $1.66\,\mathrm{W}$. This is not a frequency effect: it comes from the copper cross-section made available by the planar construction, six layers of $70\,\mu\mathrm{m}$ copper occupying the window far more efficiently than a litz bundle of equivalent height, and from the reduction of the primary leakage inductance from $540\,\mathrm{nH}$ to $21\,\mathrm{nH}$.

Third, the core-loss line must be read with care. It rises from $0.20\,\mathrm{W}$ to $1.04\,\mathrm{W}$, but the two figures are not obtained the same way: the litz value is a datasheet estimate, of the kind shown in Section IV-D to fall about a third below the element-wise result, whereas the planar value comes from the element-wise data-driven evaluation. Part of the apparent five-fold increase is therefore a method effect rather than a physical one. The same limitation prevents the frequency change from being separated from the technology change, since the baseline is characterized at $200\,\mathrm{kHz}$ and the planar design at $400\,\mathrm{kHz}$; doubling the frequency acts in opposite directions on the two mechanisms, raising the copper loss through the proximity effect while halving the flux excursion at constant turns count and applied volt-seconds. The copper comparison, which rests on measured impedances on one side and finite elements on the other, is therefore the solid part of Table VIII.

The effect at converter level is shown in Fig. 7, where the predicted efficiency of the LLC cell with the proposed transformer is compared with the efficiency measured on the existing prototype. The $4.5\,\mathrm{W}$ difference predicted for the transformer is largely recovered at full output power. Fig. 8 extends the prediction to the whole input-voltage and load range using the characterization data available for the input filter and the upstream buck-boost stage.

VI. Experimental Programme

A demonstrator of the optimized transformer is being manufactured on the qualified twelve-layer stack-up. The characterization campaign covers the DC resistance and the frequency-dependent impedance of each winding, the short-circuit impedance of each winding pair, the primary-to-secondary capacitance, a calorimetric measurement of the core loss at $400\,\mathrm{kHz}$—which is the discriminating test between the evaluation methods of Table VII—and the converter efficiency and thermal map over the full operating range.

The one-month interval between the acceptance of the digest and the manuscript deadline was not sufficient to manufacture the demonstrator and complete this campaign, which is why the present paper reports predicted rather than measured

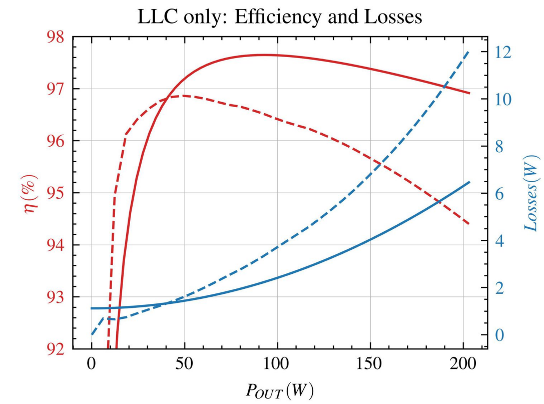

Fig. 7: Efficiency and losses of the LLC cell. Solid: proposed design with the planar transformer. Dashed: measurement on the existing prototype. Neither curve includes the transformer core loss; adding the $1.04\,\mathrm{W}$ of Table VII lowers the full-load efficiency by about 0.5 point, here and in Fig. 8.

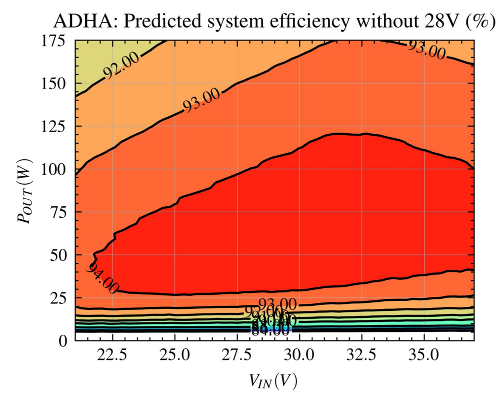

Fig. 8: Predicted system efficiency over the input-voltage and output-power range with the proposed transformer.

performance for the planar design. The measurements are in progress and **their results will be presented at the conference**.

VII. Conclusion

A planar transformer has been designed to replace the litz-wire transformer of the LLC stage of a $203\,\mathrm{W}$ multi-output space power module. The layer assignment was treated as a constrained combinatorial problem formulated on the full leakage matrix of the four-winding structure rather than on a single scalar objective, which is what the multi-output nature of the converter requires. The resulting arrangement reduces the secondary leakage inductances by more than an order of magnitude and allows the secondary snubbers to be removed.

Core losses were evaluated by applying a data-driven material model element by element to the three-dimensional flux-density map. The comparison with the datasheet and volume-averaged approaches shows that the choice of the representative flux density dominates the result on a shaped core, a point that deserves attention as neural-network material models become routine design tools.

Set against the measured litz baseline, the predicted transformer loss falls from $8.7\,\mathrm{W}$ to $4.2\,\mathrm{W}$. Once decomposed, $0.31\,\mathrm{W}$ of this reduction is attributable to the removal of the $5\,\mathrm{V}$ winding and $4.18\,\mathrm{W}$, or $49.8\,\%$ of the iso-architecture baseline, to the change of winding technology and operating frequency. The analytical pre-design underestimates this figure by $20\,\%$ and should be read as a lower bound. The improved coupling is obtained at the cost of a forty-fold increase of the primary-to-secondary capacitance; the existing common-mode filter retains $16.5\,\mathrm{dB}$ of margin, but the analysis shows that the $\mathrm{d}v/\mathrm{d}t$ pairing techniques available for single-output transformers conflict with the leakage constraints of a multi-output structure, a trade-off specific to this class of converters.

These results confirm that the direct optimization of the magnetic field distribution inside the winding window is an effective design strategy for high power density planar LLC transformers, and that it becomes a genuinely constrained problem—rather than a single minimization—under asymmetrical multi-output loading. The gains reported here remain a comparison between a measured litz reference and a predicted planar design; the experimental characterization of the demonstrator, in particular the calorimetric core-loss measurement that discriminates between the evaluation methods of Table VII, will be presented at the conference.

Acknowledgment

This work was carried out within the ADHA (Advanced Data Handling Architecture) project and is supported by the European Space Agency under contract 4000142637/23/NL/CRS. The authors thank the POWERLOGY team for its technical support throughout this work.

References

[1] P. L. Dowell, "Effects of eddy currents in transformer windings," *Proc. Inst. Electr. Eng.*, vol. 113, no. 8, pp. 1387–1394, Aug. 1966, doi: 10.1049/piee.1966.0236.

[2] J. A. Ferreira, "Improved analytical modeling of conductive losses in magnetic components," *IEEE Trans. Power Electron.*, vol. 9, no. 1, pp. 127–131, Jan. 1994, doi: 10.1109/63.285503.

[3] Z. Ouyang and M. A. E. Andersen, "Overview of planar magnetic technology—Fundamental properties," *IEEE Trans. Power Electron.*, vol. 29, no. 9, pp. 4888–4900, Sep. 2014, doi: 10.1109/TPEL.2013.2283263.

[4] Z. Ouyang, O. C. Thomsen, and M. A. E. Andersen, "The analysis and comparison of leakage inductance in different winding arrangements for planar transformer," in *Proc. IEEE Int. Conf. Power Electron. Drive Syst. (PEDS)*, 2009, pp. 1143–1148, doi: 10.1109/PEDS.2009.5385844.

[5] Z. Ouyang, O. C. Thomsen, and M. A. E. Andersen, "Optimal design and tradeoff analysis of planar transformer in high-power DC–DC converters," *IEEE Trans. Ind. Electron.*, vol. 59, no. 7, pp. 2800–2810, Jul. 2012, doi: 10.1109/TIE.2010.2046005.

[6] Z. Ouyang, W. G. Hurley, and M. A. E. Andersen, "Improved analysis and modeling of leakage inductance for planar transformers," *IEEE J. Emerg. Sel. Topics Power Electron.*, vol. 7, no. 4, pp. 2225–2231, Dec. 2019, doi: 10.1109/JESTPE.2018.2871968.

[7] D. Ba, Y. Wang, F. Yu, and X. Lyu, "Automated design of multi-layer planar transformers: An EDA tool based on a constraint-preserving genetic algorithm," *Electronics*, vol. 15, no. 11, art. no. 2392, Jun. 2026, doi: 10.3390/electronics15112392.

[8] E. Waffenschmidt and J. Jacobs, "Planar resonant multi-output transformer for printed circuit board integration," in *Proc. IEEE Power Electron. Spec. Conf. (PESC)*, 2008, pp. 4222–4228, doi: 10.1109/PESC.2008.4592619.

[9] C.-W. Park and S.-K. Han, "Analysis and design of an integrated magnetics planar transformer for high power density LLC resonant converter," *IEEE Access*, vol. 9, pp. 157499–157511, 2021, doi: 10.1109/ACCESS.2021.3125262.

[10] M. Li, C. Wang, Z. Ouyang, and M. A. E. Andersen, "Optimal design of a matrix planar transformer in an LLC resonant converter for data center applications," *IEEE J. Emerg. Sel. Topics Power Electron.*, vol. 11, no. 2, pp. 1778–1787, Apr. 2023, doi: 10.1109/JESTPE.2022.3215623.

[11] W.-J. Son and B. K. Lee, "Design of planar transformers for LLC converters in high power density on-board chargers for electric vehicles," *Energies*, vol. 16, no. 18, art. no. 6757, Sep. 2023, doi: 10.3390/en16186757.

[12] Y.-C. Liu *et al.*, "Design and implementation of a planar transformer with fractional turns for high power density LLC resonant converters," *IEEE Trans. Power Electron.*, vol. 36, no. 5, pp. 5191–5203, May 2021, doi: 10.1109/TPEL.2020.3029001.

[13] S. Zou, C. Singhabahu, J. Chen, and A. Khaligh, "A comprehensive design approach for a three-winding planar transformer," *IET Power Electron.*, vol. 15, no. 8, pp. 717–727, Jun. 2022, doi: 10.1049/pel2.12261.

[14] M. Chen *et al.*, "MagNet Challenge for data-driven power magnetics modeling," *IEEE Open J. Power Electron.*, vol. 6, pp. 883–898, 2025, doi: 10.1109/OJPEL.2024.3469916.

[15] W. Kirchgässner, N. Förster, T. Piepenbrock, O. Schweins, and O. Wallscheid, "HARDCORE: H-field and power loss estimation for arbitrary waveforms with residual, dilated convolutional neural networks in ferrite cores," *IEEE Trans. Power Electron.*, vol. 40, no. 2, pp. 3326–3335, Feb. 2025, doi: 10.1109/TPEL.2024.3488174.

[16] C. R. Sullivan, "Optimal choice for number of strands in a litz-wire transformer winding," *IEEE Trans. Power Electron.*, vol. 14, no. 2, pp. 283–291, Mar. 1999, doi: 10.1109/63.750181.

[17] M. K. Kazimierczuk, *High-Frequency Magnetic Components*, 2nd ed. Chichester, UK: Wiley, 2014.

[18] X. Huang and K. D. T. Ngo, "Design technique for a spiral planar winding with geometric radii," *IEEE Trans. Aerosp. Electron. Syst.*, vol. 32, no. 2, pp. 825–830, Apr. 1996, doi: 10.1109/7.489524.

[19] J. Mühlethaler, J. Biela, J. W. Kolar, and A. Ecklebe, "Improved core-loss calculation for magnetic components employed in power electronic systems," *IEEE Trans. Power Electron.*, vol. 27, no. 2, pp. 964–973, Feb. 2012, doi: 10.1109/TPEL.2011.2162252.

[20] H. Li, D. Serrano, S. Wang, and M. Chen, "MagNet-AI: Neural network as datasheet for magnetics modeling and material recommendation," *IEEE Trans. Power Electron.*, vol. 38, no. 12, pp. 15854–15869, Dec. 2023, doi: 10.1109/TPEL.2023.3309233.

[21] ECSS Secretariat, *Space Engineering—Electromagnetic Compatibility*, Standard ECSS-E-ST-20-07C Rev.2, ESA-ESTEC, Noordwijk, The Netherlands, Jan. 2022.

[22] M. A. Saket, M. Ordonez, and N. Shafiei, "Planar transformers with near-zero common-mode noise for flyback and forward converters," *IEEE Trans. Power Electron.*, vol. 33, no. 2, pp. 1554–1571, Feb. 2018, doi: 10.1109/TPEL.2017.2679717.

[23] M. A. Saket, M. Ordonez, M. Craciun, and C. Botting, "Common-mode noise elimination in planar transformers for LLC resonant converters," in *Proc. IEEE Energy Convers. Congr. Expo. (ECCE)*, 2018, pp. 6607–6612, doi: 10.1109/ECCE.2018.8557441.

[24] M. A. Saket, M. Ordonez, M. Craciun, and C. Botting, "Improving planar transformers for LLC resonant converters: Paired layers interleaving," *IEEE Trans. Power Electron.*, vol. 34, no. 12, pp. 11813–11832, Dec. 2019, doi: 10.1109/TPEL.2019.2903168.

[25] R. Bakri, G. Corgne, and X. Margueron, "Thermal modeling of planar magnetics: Fundamentals, review and key points," *IEEE Access*, vol. 11, pp. 41654–41679, 2023, doi: 10.1109/ACCESS.2023.3269662.

[26] G. Salinas, J. A. Oliver, J. Munoz-Anton, A. Fernandez, and R. Prieto, "Thermal management of planar magnetics for spacecrafts: Characterization and modeling," in *Proc. Eur. Space Power Conf. (ESPC)*, 2019, pp. 1–6, doi: 10.1109/ESPC.2019.8932068.